Systematic Design of the Hybrid Damping Method for Three-Phase Inverters With *High-Order* Filters

Jie Ye, Anwen Shen, Zhixiong Zhang, Jinbang Xu, and Fang Wu

***Abstract*—*High-order* filters (*HO*-filters) such as *LCL-LC*-filters have recently drawn attention to their small size and better attenuation to switching harmonics than *LCL*-filters for three-phase inverter grid interfaces. Hybrid damping that combines passive damping and active damping is an effective method to suppress *HO*-filter resonances. However, due to the high-order characteristic of the system, the tuning procedure for the parameters of hybrid damping is complicated. Hence, an equivalent circuit analysis method is proposed in this paper to accurately simplify the model of the *HO*-filter. Based on this, a systematic step-by-step design method for *HO*-filter-type grid-connected inverters with hybrid damping has been proposed. The passive losses, effects of equivalent series resistances (ESRs) and robustness against grid impedance variation have been studied. Compared with existing design procedures, the proposed method makes the hybrid damping more reliable by locating appropriate position for closed-loop resonant poles. Experimental results verify the proposed systematic design procedure.**

***Index Terms*—Grid-connected inverter, hybrid damping, high-order (HO) filter, parameter design, three phase.**

I. Introduction

RECENTLY, due to the energy crisis, distributed generation (DG) systems using clean renewable energy have become an important topic in technical research. As an interface between a DG system and a power grid, a grid-connected inverter plays an important role in injecting high-quality power into the grid [1]. A low-pass passive filter (typical *LCL*-filter) is often inserted between the inverter and the grid to attenuate the pulse width modulation (PWM) carrier and sideband harmonics injected into the point of common coupling [2]. Due to the increasing price of copper, inductors become more and more expensive, particularly for the ones with large inductance and high current capacity. Therefore, many *high-order* filters (*HO*-filters) based on the *LCL*-filter were proposed to achieve better harmonic rejection and reduce the total cost of the inductors [3], [4]. However, more complex resonant problems cause more control problems for the *HO*-filter-based grid-connected inverters.

An *RC* damper, which is in parallel with the capacitor branch is often adopted due to its small additional power losses [5]–[7]. It is found that the passive damping is not affected by the controller parameters and processing delay. However, the effectiveness of this method depends on specific grid condition [8]. Alternatively, multiloop- and single-loop filter-based active damping techniques were developed to eliminate the resonant peaks instead of adding any passive dampers. In the multiloop-based damping, more system state variables are involved into the control loop to guarantee the system stability, such as the virtual resistor [9], the capacitor voltage feedback [10], [11], and the capacitor current feedback [12]–[16]. It means that two or even more control loops are required to damp the system resonant peaks. This kind of damping method is sensitive to the processing delay and may introduce right-half-plane open-loop poles into the system [17]. Some sensorless estimation methods have been proposed to obtain the information like the capacitor current [15] and voltage [11]. These algorithms require accurate sampling of the inverter-side current, and some adverse impacts on the overall performance may be introduced when the system model is not accurate [15]. In the single-loop filter-based damping methods, a higher order digital filter is used in the forward path of the current control loop to regulate the low-frequency dynamics and damp the potentially unstable high-frequency dynamics [18]–[21]. It acted like filtering the resonant peak in the manner of the open-loop control. This kind of active damping methods has the advantage of fewer sensors. In addition, the study in [21] indicated that the effectiveness of the filter-based damping method depends on the accuracy of the system model.

Hybrid damping addresses these limitations to enhance dynamic response, stability margin, and damping performance of the system by rationally combining the advantages of both passive damping and active damping. This type of damping method has been discussed in [8] and [22]. The proper design of the hybrid damping parameters is essentially to achieve effective resonance damping. However, few of literatures to date precisely analyzed the hybrid damping method used in *HO*-filter-based inverters, particularly when the inverter current feedback is adopted. In most of the existing design methods, the damping parameters need to be chosen according to specific open-loop gain margin or phase margin. When open-loop unstable poles exist, multiple stable margins must be investigated. Therefore, the optimum performance of hybrid damping may not be guaranteed by specific stability margin. Moreover, the resonant

Manuscript received March 25, 2016; revised May 24, 2016, July 5, 2016, September 27, 2016, and October 31, 2016; accepted December 1, 2016. Date of publication December 8, 2016; date of current version February 22, 2018. This work was supported by the Natural Science Foundation of China under Grant 61472154. Recommended by for publication by Associated Editor M. T. Bina. *(Corresponding author: Zhixiong Zhang.)*

The authors are with the Key Laboratory of Electronic Power and Power Transformation, School of Automation, Huazhong University of Science and Technology, Wuhan 430074, China (e-mail: yejiehust@foxmail.com; sawyi@mail.hust.edu.cn; zzxhust@foxmail.com; jbxuhust@gmail.com; kenny334@hust.edu.cn).

Color versions of one or more of the figures in this paper are available online at http://ieeexplore.ieee.org.

Digital Object Identifier 10.1109/TPEL.2016.2637377

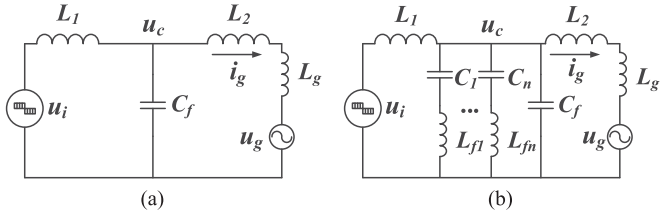

Fig. 1. Topologies of the line-side filter. (a) *LCL*-filter. (b) *HO* trap filter.

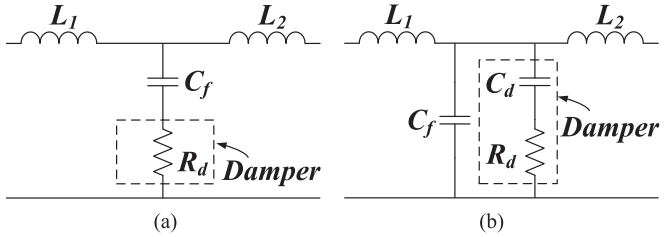

Fig. 2. Different passive damping solutions. (a) *RC*-series passive damping. (b) *RC*-parallel passive damping.

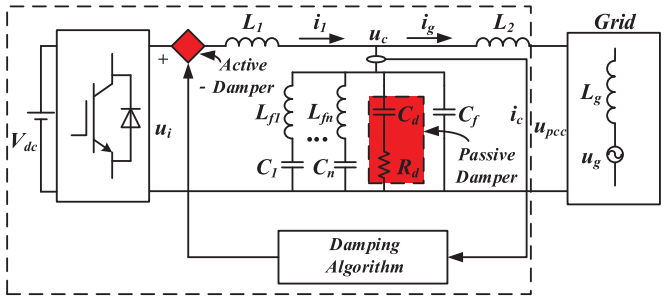

Fig. 3. Three-phase *HO*-filtered grid-connected inverter based on hybrid damping.

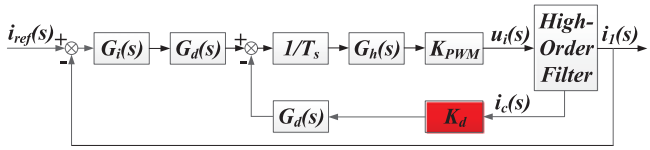

Fig. 4. Mathematical model of the digitally controlled *HO*-filter-type inverter with filter current feedback active damping.

frequency varies with different damping parameters, so the design of the damping parameters becomes challenging.

This paper proposes a systematic design method for the *HO*-filter-based inverter with hybrid damping to deal with these problems. The rest of this paper is organized as follows. In Section II, different *HO*-filter topologies are described, and the mathematical model of the *HO*-filter-type grid-connected inverter using averaged switch model (ASM) is derived. Based on these topologies and the ASM, the equivalent circuit analysis method for the *HO*-filter and a step-by-step optimal design method are given in Section III. In Section IV, a design example is illustrated to make an intuitive understanding of the proposed design method. Finally, in Section V, experiments on a 65-kW prototype are performed to validate the theoretical analysis in the previous sections, and concluded in Section VI.

II. Filter Topologies and Modeling of the Digitally Controlled Inverter

A. Filter Topologies

The most commonly used line-side filter topology would be the *LCL*-filter illustrated in Fig. 1(a). Fig. 1(b) shows the topology of the *HO*-filter, which uses an *LC* series resonant circuit working at the switching frequency or multiples of switching frequencies. The line-side *HO*-filter is composed of inverter-side inductor L_1, grid-side inductor L_2, filter capacitor C_f, resonant capacitors $C_1, C_2, \ldots, C_n$, and resonant inductors $L_{f1}, L_{f2}, \ldots, L_{fn}$. u_i is the inverter output voltage; u_c is the filter voltage; u_g is the grid voltage, and i_g is the grid current. The multiple $L_{fn} - C_n$ trap filter branches compose multiple series resonant circuits to achieve zero impedance at the selected frequencies, and the single branch of the capacitor (C_f) guarantees -60 dB/decade attenuation in the high-frequency band.

An *RC*-parallel passive damping as shown in Fig. 2(b) was proven to be efficient and effective over series damping [5] [see Fig. 2(a)]. Compared with the series damping method, the advantage of this method is that the damping branch does not jeopardize the high harmonic suppression of the filter. This paper uses *RC*-parallel damping topology as the passive part of the hybrid solution. In order to facilitate the following description, the transfer function $u_c(s)/u_i(s)$ of the *LCL*-filter with *RC*-parallel damping is presented as

$$G_{LCL}(s) = \frac{C_d R_d L_t s + L_t}{(As^3 + Bs^2 + Cs + D)} \tag{1}$$

where the total grid inductance $L_t = L_2 + L_g$ and the parameters in the denominator are as follows:

$$\begin{cases} A = C_d C_f L_1 L_t R_d \\ B = C_d L_1 L_t + C_f L_1 L_t \\ C = C_d L_1 R_d + C_d L_t R_d \\ D = L_1 + L_t. \end{cases}$$

B. Modeling of the Digitally Controlled Inverter

Fig. 3 shows a generic structure of the *HO*-filter-based grid-connected inverter with hybrid damping. For simplicity, the equivalent series resistances (ESRs) of the inverter side inductor $L_1(R_1)$ and grid side inductor $L_2(R_2)$ are ignored in the design procedure. In fact, any practical ESRs will only damp the resonance, making the system more stable. The ESRs are neglected here to emulate the worst operating conditions. Among the various active damping solutions, the filter current feedback active damping has been widely used for its simpleness, flexibility, and effectiveness, and it is chosen as the active part of the hybrid solution.

As shown in Fig. 4, the inverter-side current i_1 is conventionally used as the feedback of a current controller to regulate the current injected into the grid.

A PR regulator is employed and tuned considering the overall system dynamics, which are mainly evaluated by the unity-gain crossover frequency and the phase margin [13]. In s-domain,

the PR regulator is expressed as

$$G_i(s) = K_p + \frac{2K_r\omega_i s}{s^2 + 2\omega_i s + \omega_0^2} \tag{2}$$

where ω_i is the resonant cutoff frequency, and K_p and K_r are the proportional and resonant gain, respectively. To deal with a typical $\pm 1\%$ variation of the grid fundamental angular frequency ω_0 [23], $\omega_i = 1\% \cdot \omega_0$ rad/s is set.

A computation delay is introduced into the current loop. The one-sample computation delay is

$$G_d(s) = e^{-sT_s} \tag{3}$$

where T_s is the sampling period.

Sampling is inherent in the z-domain analysis, but if the purpose is to model a discrete system as a continuous system, the sampler $1/T_s$ has to be taken into account. The continuous expression of the zero-order hold is expressed as

$$G_h(s) = \frac{1 - e^{-sT_s}}{s}. \tag{4}$$

In order to obtain rational transfer functions, delays are usually approximated by poles and zeros. One of the most popular approximations for delays is the *Padé* approximation [24]. It attains accurate approximation within the range of the crossover frequency and the *Nyquist* frequency.

$$e^{-sT_s} \approx \frac{1 - 0.5 \cdot s \cdot T_s}{1 + 0.5 \cdot s \cdot T_s}. \tag{5}$$

K_{PWM} is the transfer function of the PWM inverter, always expressed as 1. Meanwhile, K_d is the filter current feedback coefficient.

III. Systematic Parameters Design Method of the Hybrid Damping Strategy

A. Equivalent Circuit Analysis Method

The purpose of the damping is to reduce the *Q-factor* at the characteristic resonant frequency. One factor needs to be noted is that there are multiple characteristic resonant frequencies for the *HO*-filter and any practical ESRs will damp the higher frequency resonances well. Thus, the higher frequency resonances do not need to be considered here. For the *HO*-filter, to find out the optimized *Q-factor*, the exact characteristic resonant frequency should be obtained by calculating the complex conjugate solutions of the high-order characteristic equation of the transfer function $u_c(s)/u_i(s)$. And it is difficult to get the solutions.

From the perspective of filter design, one basic limit on the parameters was discussed in [2] and [25]. That is, the first characteristic resonant frequency of the *HO*-filter should be in the range between system crossover frequency and one half of the switching frequency, in order to avoid resonant problems in the lowest and highest parts of the harmonic spectrum. The impedances $Z_{\mathrm{eqi}}(s)$ $(i = 1, \ldots, n)$ of the trap branches at the characteristic resonant frequency are calculated as

$$Z_{\mathrm{eqi}}(j\omega_r^{HO}) = \frac{1 - L_{fi}C_i{\omega_r^{HO}}^2}{C_i\omega_r^{HO}j} \tag{6}$$

where ω_r^{HO} is the first characteristic resonant frequency of the *HO*-filter.

The *LC* resonant frequencies of trap branches are derived as $\omega_{\mathrm{trap\_ri}} = 1/\sqrt{L_{fi}C_i}$, and the equivalent capacitance C_{eqi} of the trap branches at the characteristic resonant frequency can be deduced as

$$\frac{1}{jC_{\mathrm{eqi}}\omega_r^{HO}} = \frac{1 - L_{fi}C_i{\omega_r^{HO}}^2}{C_i\omega_r^{HO}j}$$

$$C_{\mathrm{eqi}} = \frac{C_i}{1 - \left(\frac{\omega_r^{HO}}{\omega_{\mathrm{trap\_ri}}}\right)^2}. \tag{7}$$

According to the aforementioned derivation, the *HO*-filter can be simplified into an *LCL*-filter when working at the characteristic resonant frequency or lower. The capacitance $C^{'}$ of the equivalent *LCL*-filter should be set as the sum of the equivalent capacitance of each trap branch and C_f.

$$C^{'} = C_f + C_{\mathrm{eq1}} + C_{\mathrm{eq2}} + \cdots + C_{\mathrm{eqn}}. \tag{8}$$

Ignore (7) temporarily, let

$$C_{\mathrm{eqi}} = C_i \tag{9}$$

then the resonant frequency of the equivalent *LCL*-filter, which is simplified by (9) under the stiffest grid ($L_g = 0$) can be calculated as

$$\omega_{r0}^{LCL} = \sqrt{\frac{L_1 + L_2}{L_1L_2(C_f + C_1 + C_2 + \cdots + C_n)}}. \tag{10}$$

It can be seen from (7) that C_{eqi} is larger than C_i. Therefore, the resonant frequency of the *HO*-filter is slightly smaller than that of the equivalent *LCL*-filter simplified by (9). Substituting ω_{r0}^{LCL} into the transfer function $u_c(s)/u_i(s)$ of the *HO*-filter without damping, and progressively decreasing ω_{r0}^{LCL}, we can obtain the resonant frequency of the *HO*-filter ω_{r0}^{HO} under the stiffest grid. The decrease length is selected as 10 Hz. ω_{r0}^{HO} is detected by observing a reduction in the loop gain of the *HO*-filter for decreasing ω_{r0}^{LCL}. Finally, the equivalent capacitance C_{eqi} can be calculated by substituting ω_{r0}^{HO} into (7).

The *HO*-filter and the equivalent *LCL*-filter have almost the same resonant frequency and response curve at mid frequency band or lower frequency band since the traps affect mainly the high frequency range of the filter (well above the resonant frequency of the filter) as shown in Fig. 5.

Both of the two filters have the same *RC*-parallel damping branch. Therefore, the *Q-factor* of the *HO*-filter at the first characteristic resonant frequency can be defined [6] and approximately obtained using

$$Q = \frac{|G_{HO}(j\omega_r^{HO})|}{|G_{HO}(j0)|} \approx \frac{|G_{LCL}(j\omega_r^{LCL})|}{|G_{LCL}(j0)|} \tag{11}$$

where ω_r^{LCL} represents the first resonant angular frequency of the *LCL*-filter and $G_{HO}(s)$ represents the transfer function $u_c(s)/u_i(s)$ of the *HO*-filter with *RC*-parallel damping.

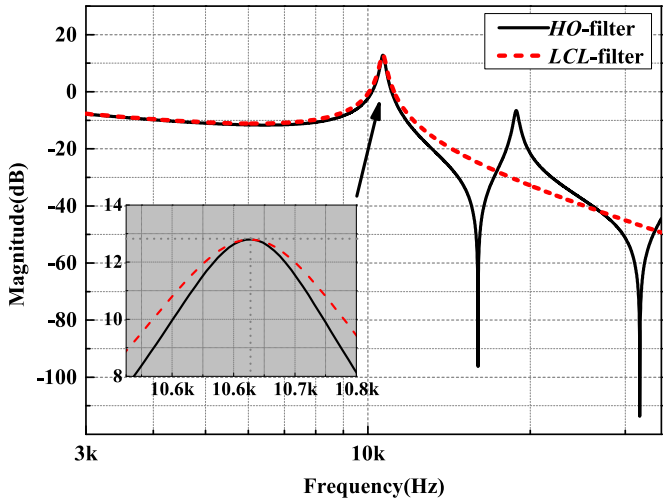

Fig. 5. Bode plots of $u_c(s)/u_i(s)$ of *HO*-filter and its equivalent *LCL*-filter.

B. Analyzing the Effect of the Capacitance of Passive Damping Branch on Power Loss and Damping

At present, the most commonly used PWM methods with low harmonic distortion for the three-phase two-level inverter are the sine-triangle symmetrical regular PWM (SSPWM), the sine-triangle asymmetrical regular PWM (ASSPWM), the symmetrical regular sampled space vector modulation (SSVPWM), and the asymmetrical regular sampled space vector modulation (ASSVPWM). The significant switching harmonics of the inverter output voltage u_i contain components at the frequencies around $f_{\rm sw}$ ($f_{\rm sw}$ is the switching frequency) and $2f_{\rm sw}$ for all of these four PWM methods, and the main difference between them lies in sideband harmonic components [26]. For example, when the inverter is operated under the condition of ASSPWM, the switching harmonics amplitude of the inverter output voltage $U_{\rm AM}(m,n)$ can be written as follows [26]:

$$U_{\rm AM}(m,n)\Big|_{\substack{m=1,2,\ldots,\infty\\ n=\pm1,\pm2,\ldots,\pm\infty}} = \frac{8V_{\rm dc}}{3\pi q} J_n\left(q\frac{\pi}{2}M\right)\cdot\sin\left[(m+n)\frac{\pi}{2}\right]\sin^2\left(\frac{\pi}{3}n\right) \tag{12}$$

where M is the modulation index, $V_{\rm dc}$ is the dc link voltage, m is the carrier index, n is the baseband index, q represents $[m+n(f_0/f_{\rm sw})]$, f_0 represents the grid fundamental frequency, and $J_n(x)$ is referred as the integrals of the Bessel function, which is expressed as $J_n(x) = (1/2\pi)\int_0^{2\pi}\cos(n\tau - x\sin\tau)d\tau$, showing the different sideband harmonic magnitudes. The odd harmonic sideband components around odd multiples of the carrier fundamental and even harmonic sideband components around even multiples of the carrier fundamental are completely eliminated. The significant switching harmonics of the inverter output voltage occur at the frequencies of $f_{\rm sw}\pm 2f_0$, $2f_{\rm sw}\pm f_0$. Similarly, the analytical solutions for $U_{\rm AM}(m,n)$ of other PWM methods can be found in [26], and are not repeated here.

Expressions for the fundamental and the harmonics power losses are given based on [6] and modified to improve accuracy.

1) Fundamental Frequency Power Loss: The power loss of the damping circuit for the fundamental frequency is

$$P_d(\text{fun}) = \frac{U_c^2\omega_0^2 C_d^2 R_d}{1+\omega_0^2 C_d^2 R_d^2} \tag{13}$$

where U_c is the rms value of filter voltage, and U_c is equal to the rms value of grid voltage.

2) Harmonics Power Loss: The grid is assumed to be an ideal voltage source at the fundamental frequency, and it will become a short circuit at higher frequency. From the transfer function $u_c(s)/u_i(s)$ of the *HO*-filter

$$\begin{aligned} P_d(\omega_{mf_{\rm sw}+nf_0}) &= \text{Real}\left[U_c\left(U_c\frac{\omega_{\rm sw}C_d(\omega_{\rm sw}C_dR_d+j)}{1+\omega_{\rm sw}^2C_d^2R_d^2}\right)^*\right] \\ &= \text{Real}\left[\frac{U_{\rm AM}^2(m,n)}{2}\frac{u_c(j\omega_{mf_{\rm sw}+nf_0})}{u_i(j\omega_{mf_{\rm sw}+nf_0})}\cdot\left[\frac{u_c(j\omega_{mf_{\rm sw}+nf_0})}{u_i(j\omega_{mf_{\rm sw}+nf_0})}\right]^*\frac{\omega_{mf_{\rm sw}+nf_0}^2C_d^2R_d}{1+\omega_{mf_{\rm sw}+nf_0}^2C_d^2R_d^2}\right] \end{aligned} \tag{14}$$

where $\omega_{mf_{\rm sw}+nf_0}$ represents the radian frequency of switching harmonics. The total power losses in the damping circuit with different PWM methods can be derived as

$$\begin{aligned} \text{SSPWM}: P_d(\text{total}) &= P_d(\text{fun}) + P_d(\omega_{f_{\rm sw}\pm f_0}) + P_d(\omega_{f_{\rm sw}\pm 2f_0}) + P_d(\omega_{2f_{\rm sw}\pm f_0}) \\ \text{ASSPWM}: P_d(\text{total}) &= P_d(\text{fun}) + P_d(\omega_{f_{\rm sw}\pm 2f_0}) + P_d(\omega_{2f_{\rm sw}\pm f_0}) \\ \text{SSVPWM}: P_d(\text{total}) &= P_d(\text{fun}) + P_d(\omega_{f_{\rm sw}\pm f_0}) + P_d(\omega_{f_{\rm sw}\pm 2f_0}) + P_d(\omega_{f_{\rm sw}\pm 4f_0}) + P_d(\omega_{2f_{\rm sw}\pm f_0}) \\ \text{ASSVPWM}: P_d(\text{total}) &= P_d(\text{fun}) + P_d(\omega_{f_{\rm sw}\pm 2f_0}) + P_d(\omega_{f_{\rm sw}\pm 4f_0}) + P_d(\omega_{2f_{\rm sw}\pm f_0}). \end{aligned} \tag{15}$$

The selection of C_d/C_f is a tradeoff between effective damping and power losses in the shunt damping circuit. Let

$$C_d = a_C\cdot C_f. \tag{16}$$

In order to analyze the effect of a_C on the damping, we use the *Q-factor*. The exact characteristic resonant frequency of the equivalent *LCL*-filter can be obtained by solving the complex conjugate roots of third-order characteristic equation in (1). It can be derived as

$$\omega_r^{LCL} = |r_p| = \left|\frac{F}{6A} - \frac{6AC-2B^2}{3AF} - \frac{B}{3A}\right| \tag{17}$$

where $F = (-108A^2D + 36ABC + 12\sqrt{3}AG - 8B^3)^{1/3}$, $G = \sqrt{27A^2D^2 - 18ABCD + 4AC^3 + 4B^3D - B^2C^2}$, and r_p represents one of the complex conjugate roots.

Equation (11) can be derived in terms of a_C. Fig. 6 shows the variation of *Q-factor* and power loss, w.r.t., a_C for different R_d values. It should be noted from Fig. 6 that *Q-factor* cannot be reduced indefinitely by selecting very high value of a_C. All

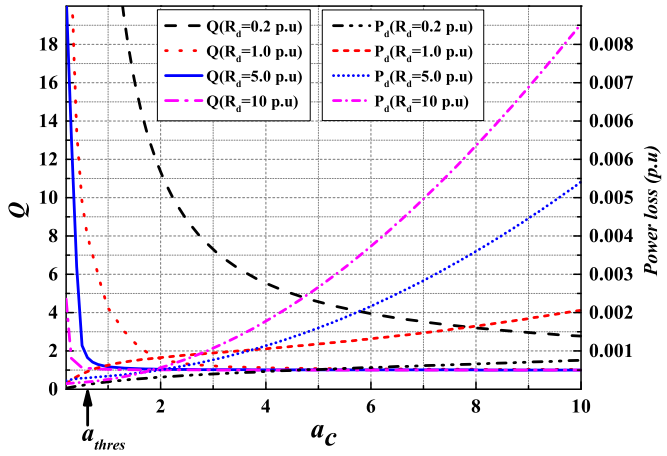

Fig. 6. *Q-factor* and total power dissipation in per unit for the damping branch of the *HO*-filter.

the power loss curves show a clear upward trend, which clearly indicates that a higher value of a_C is not an efficient choice. The damping performance does not show significant improvement beyond a certain point on each of the curves.

C. Analyzing the Influence of Delay on Damping

The digital implementation of the capacitor current feedback incorporates lagging phase shifts due to the computational and PWM delays. A comprehensive investigation of the effect of the computational delay has been done in [27]. However, for the sake of the readability, a brief review is given in this paper. The effect of the computational and PWM delays at the resonant frequency can be represented by

$$\frac{G_d(j\omega_r^{HO})G_h(j\omega_r^{HO})}{T_s} = e^{-jT_s\omega_r^{HO}}\frac{1-e^{-jT_s\omega_r^{HO}}}{jT_s\omega_r^{HO}} \tag{18}$$

which can be factorized as

$$\frac{G_d(j\omega_r^{HO})G_h(j\omega_r^{HO})}{T_s} = e^{-j\frac{3}{2}T_s\omega_r^{HO}}\,\mathrm{sinc}\left(\frac{T_s\omega_r^{HO}}{2}\right). \tag{19}$$

Separating the real and imaginary components of (19) with K_d

$$K_d\frac{G_d(j\omega_r^{HO})G_h(j\omega_r^{HO})}{T_s} = K_d\mathrm{sinc}\left(\frac{T_s\omega_r^{HO}}{2}\right) \times\left[\cos\left(-\frac{3T_s\omega_r^{HO}}{2}\right) + j\sin\left(-\frac{3T_s\omega_r^{HO}}{2}\right)\right]. \tag{20}$$

The only feedback component of (20) that produces active damping is the real part, which is in phase with the capacitor current at the resonance frequency. Therefore, the condition to obtain active damping is

$$K_d\mathrm{sinc}\left(\frac{\omega_r^{HO}}{2f_s}\right)\cos\left(\frac{3\omega_r^{HO}}{2f_s}\right) > 0 \tag{21}$$

where f_s represents the sampling frequency. In order to make (21) positive up to maximum ratio $f_s/f_r = 6$ ($f_r = \omega_r^{HO}/(2\pi)$), the gain K_d should be negative. For higher f_s/f_r, the gain K_d must be positive to fulfill (21), and the delays can be considered negligible.

D. Design Procedure

The systematic design method includes the following five steps.

Step 1—Design the Passive Damper: First of all, we need to determine the number of trap filter branches and the *LC* resonant frequency of each branch. Based on the equivalent circuit analysis method, the *HO*-filter is simplified as an *LCL*-filter. The equivalent capacitance can be derived using (8).

With the equivalent *LCL*-filter parameters and different values of R_d, multiple diagrams that reflect the variation of *Q-factor* and power loss, w.r.t., a_C can be obtained. As shown in Fig. 6, there is no improvement in the *Q-factor* if a_C is increased beyond a certain value a_{thres}. Therefore, we can set a_C based on a_{thres} and the complexity of actual capacitor configuration. The similar selecting method is also discussed in [6].

According to [5], the resistance R_d is limited within the range of

$$\frac{1}{R_dC_d} \le \left|\frac{F}{6A} - \frac{6AC-2B^2}{3AF} - \frac{B}{3A}\right| \le \frac{C_d+C'}{R_dC_dC'}. \tag{22}$$

The value of R_d is localized in $[R_{\min}, +\infty)$. The upper bound is limited by the power loss. So, $R_d = R_{\min}$ is chosen for reducing power consumption as much as possible.

According to Section III-C, the delay and active damping have no prominent influence on the system stability under the weakest grid ($f_s/f_r > 6$) unless a large positive value of K_d is adopted, which contradicts the case under the stiffest grid condition ($f_s/f_r < 6$). Therefore, the sufficient stability cannot be guaranteed by active damping under the weakest grid. Therefore, the resistor of the passive damper is suggested to be designed under the weakest grid condition.

Step 2—Determine the Parameters of the PR Regulator: The system studied in this paper has a high-order transfer function, and several phase margins at different frequencies can occur. However, recognizing that the magnitude and phase contribution of the resonance is going to be small at the lowest crossover frequency ω_c, the plant response will always be dominated by the series inductance. Hence, only the low-frequency component of the plant is required, which makes the filter like a simple inductor. Thus, the design method of the PR regulator described in [28] is applicable in this case. Another point needs to be noted from [25] is that control bandwidth cannot exceed or even be close to the resonant frequency since it will create a 180° phase lag, limiting the system crossover frequency ω_c to be less than 0.3 times the resonant frequency. In order to keep the whole system stable, the crossover frequency of the plant is set as 0.3 times the resonant frequency under the stiffest grid condition. As described in [28], the maximum possible magnitude of K_p can now be found by setting the open loop gain at this value of ω_c to unity, which gives

$$K_p \approx \omega_c(L_1+L_2). \tag{23}$$

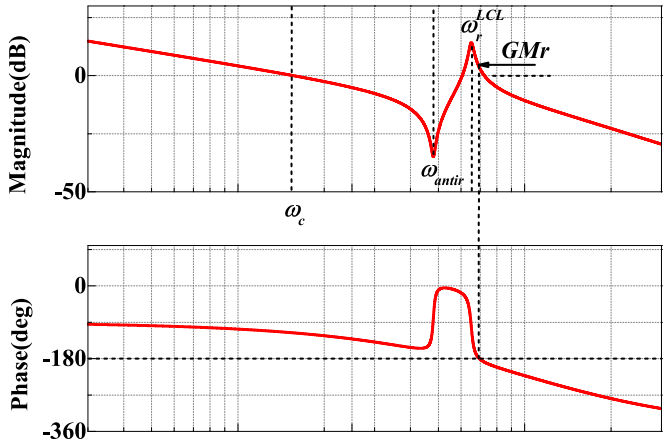

Fig. 7. Bode plot of open-loop transfer function of the equivalent *LCL*-based inverter.

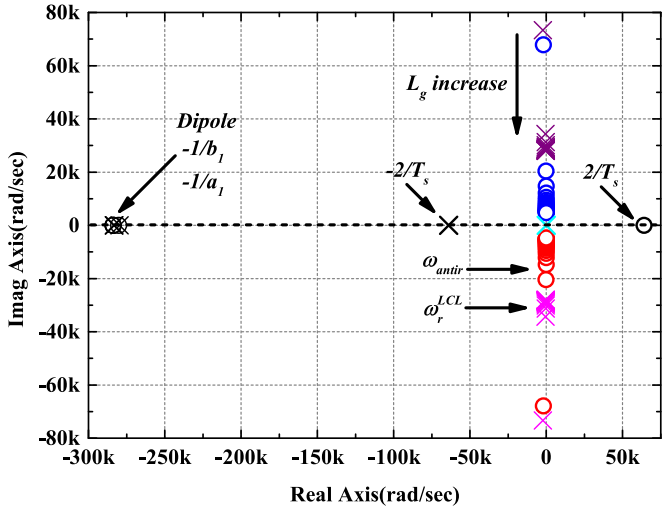

Fig. 8. Open-loop pole-zero maps of the equivalent *LCL*-based inverter with increased grid impedance.

Then, K_r can be approximately derived by

$$K_r \approx \frac{K_p \omega_c}{10}. \tag{24}$$

Step 3—Determine the Critical Grid Inductance: For the *RC*-parallel damped system, the minimum stability margin occurs at critical grid inductance. In order to obtain the critical grid inductance, the work in [29] used the Hessian matrix of the gain of the open-loop transfer function to derive the critical frequency. However, the local gain around the resonant frequency will continuously increase with the increased grid inductance when inverter-side current is used as the feedback of a current controller. The is because the conjugate zeros of the open-loop transfer function of the inverter-current feedback introduce a negative peak and cause less damping at ω_r^{LCL} as they compensate the effect of two resonant poles as shown in Fig. 7. *GMr* represents the gain margin around the resonance.

Therefore, with the impact of conjugate zeros considered, $|G_{\rm open}(j\omega_r^{LCL})G_{\rm open}(j\omega_{\rm antir})|$ can be used to investigate the stability margin along with the variation of grid impedance, where $\omega_{\rm antir}$ represents the antiresonance frequency.

The expressions of the open-loop transfer function $G_{\rm open}(s)$ of the *RC*-parallel damped system can be factored as

$$\begin{aligned} G_{\rm open}(s) &= \frac{K_p G_d(s) G_h(s)\,[1 - G_{LCL}(s)]}{T_s L_1 s} \\ &= \frac{(a_1 s + 1)(s^2 + 2\xi_1 \omega_{\rm antir} s + \omega_{\rm antir}^2)(s - \frac{2}{T_s})}{s(s + \frac{2}{T_s})^2 (s^2 + 2\xi_2 \omega_r^{LCL} s + \omega_r^{LCL\,2})(b_1 s + 1)} \end{aligned} \tag{25}$$

where ξ_1 and ξ_2 represent the damping factor of the open-loop zeros and poles, respectively, $-1/a_1$ represents the open-loop zero on the real axis and $-1/b_1$ represents the open-loop pole on the real axis. $G_i(s)$ is represented by a proportional gain K_p. This is due to the fact that a PI and PR regulator can be reduced to a proportional gain after crossover frequency ω_c [16]. ξ_2 can be calculated as

$$\xi_2 = |\text{Real}[r_p]|/\omega_r^{LCL}. \tag{26}$$

Then, b_1 can be easily determined by a certain open-loop transfer function. The open-loop zero-pole map with increased grid impedance is depicted in Fig. 8. a_1 is approximately equal to b_1 due to the existence of a pair of open-loop dipole. Thus, ξ_1 and $\omega_{\rm antir}$ can be obtained by solving the complex conjugate roots of second-order characteristic equation. The derivative of $|G_{\rm open}(j\omega_r^{LCL})G_{\rm open}(j\omega_{\rm antir})|$ with respect to the grid inductance results in the critical grid inductance as indicated by

$$\frac{d}{d(L_t)} |G_{\rm open}(j\omega_r^{LCL})G_{\rm open}(j\omega_{\rm antir})| = 0. \tag{27}$$

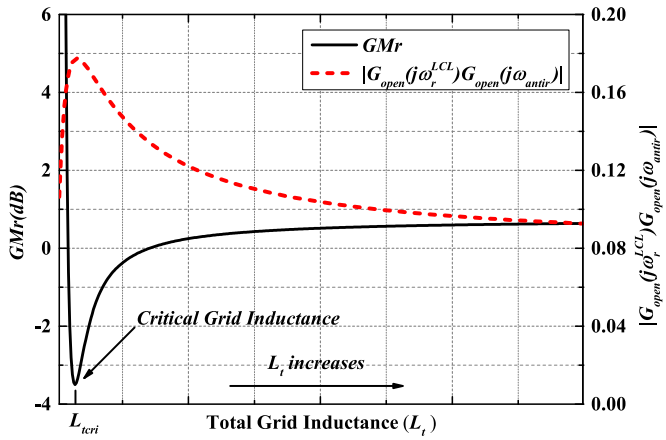

Fig. 9. Curves of $|G_{\rm open}(j\omega_r^{LCL})G_{\rm open}(j\omega_{\rm antir})|$ and *GMr* with the increase in L_t.

The stability of the *RC*-parallel damped system is determined by the gain margin *GMr* around the resonant frequency as shown in Fig. 7 since there is no open-loop unstable pole. The variations of $|G_{\rm open}(j\omega_r^{LCL})G_{\rm open}(j\omega_{\rm antir})|$ and *GMr* as function of L_t are illustrated in Fig. 9. It can be seen that the maximum value of $|G_{\rm open}(j\omega_r^{LCL})G_{\rm open}(j\omega_{\rm antir})|$ occurs at critical grid inductance $L_{\rm tcri}$ (minimum gain margin). This phenomenon verifies the correctness of the calculation method. In case the L_2 is large enough, (27) is not valid and the critical grid inductance $L_{\rm tcri}$ is equal to L_2.

Step 4—Determine the Filter-Current-Feedback Coefficient: As mentioned before, the influence of active damping is lim-

ited under the weakest grid condition, and the stability is mainly provided by the passive damping. Moreover, the stability margin is large enough under the stiffest grid condition. Therefore, K_d should be designed under the critical grid condition.

The denominator of the closed-loop transfer function of the hybrid damped system can be written as

$$\mathrm{Den}(s) = d_1 s^6 + d_2 s^5 + d_3 s^4 + d_4 s^3 + d_5 s^2 + d_6 s + 4K_p \tag{28}$$

where the parameters are as follows:

$$\begin{cases} d_1 = C_d C_f' L_1 L_t R_d T_s^2 \\ d_2 = 4C_d C_f' L_1 L_t R_d T_s + L_1 L_t T_s^2 (C_d + C_f') \\ d_3 = -2C_d C_f' L_t R_d T_s (K_d + K_p) + 4C_d C_f' L_1 L_t R_d \\ \quad + C_d R_d T_s^2 (L_1 + L_t) + 4L_1 L_t T_s (C_d + C_f') \\ d_4 = 4C_d C_f' L_t R_d (K_d + K_p) + 4L_1 L_t (C_f' + C_d) \\ \quad + (T_s + 4C_d R_d)(L_1 + L_t) T_s \\ \quad - 2L_t T_s (C_d + C_f')(K_p + K_d) \\ d_5 = -2C_d K_p R_d T_s + 4L_t (K_p + K_d)(C_f' + C_d) \\ \quad + 4C_d R_d (L_1 + L_t) + 4L_1 T_s + 4L_t T_s \\ d_6 = 4C_d K_p R_d - 2K_p T_s + 4L_1 + 4L_t. \end{cases}$$

In fact, the stability of the *HO*-filter-type inverter is depends on the damping factor ξ_{cl} of the closed-loop resonant pole pair which are the closest poles to the imaginary axis of s-domain (the pair of closed-loop poles introduced by the PR controller is not considered here). The optimum results are presented in [7], [10], [13], [18], and [19], and the value of ξ_{cl} is near 0.1, which means the system has good stability. To obtain the desired ξ_{cl}, we define

$$s' = s + \omega_r^{LCL} \xi_{\mathrm{cl}}. \tag{29}$$

where ω_r^{LCL} is used to approximate the closed-loop resonant frequency ω_r^{cl}. Substituting (29) into (28)

$$\begin{aligned} \mathrm{Den}(s') = {} & d_1 (s' - \omega_r^{LCL} \xi_{\mathrm{cl}})^6 + d_2 (s' - \omega_r^{LCL} \xi_{\mathrm{cl}})^5 \\ & + d_3 (s' - \omega_r^{LCL} \xi_{\mathrm{cl}})^4 + d_4 (s' - \omega_r^{LCL} \xi_{\mathrm{cl}})^3 \\ & + d_5 (s' - \omega_r^{LCL} \xi_{\mathrm{cl}})^2 + d_6 (s' - \omega_r^{LCL} \xi_{\mathrm{cl}}) + d_7. \end{aligned} \tag{30}$$

In order to maximize the damping of the closed-loop resonant poles, a pole localization method is adopted in this paper as shown in Fig. 10. Considering the error between ω_r^{LCL} and the closed-loop resonant frequency ω_r^{cl}, the algorithm starts from $\xi_{\mathrm{cl}} = 0.2$. Applying the Routh's method to (30), the algorithm determines whether a range of K_d exists; if not, the algorithm progressively decreases the damping factor ξ_{cl} until the range of K_d exists. The decrement step for the searching is selected as 0.01. It only takes a few steps for the algorithm to obtain the satisfactory range of K_d.

A narrow range of K_d can be derived using this algorithm and the optimal K_d can be easily picked out. In case the pole on real axis is closer to imaginary axis than the resonant poles due to a large grid inductance, this method is still applicable. This is mainly because the position of the pole on real axis changes little even if K_d varies in a wide range under the weakest grid condition.

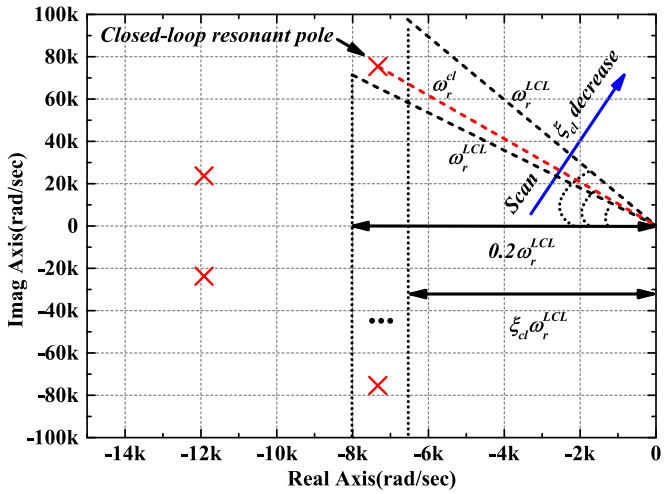

Fig. 10. Damping-factor-based pole localization method.

Step 5—Checking the Stability of Hybrid Damped System: The same with the equivalent *LCL*-based system, the minimum damping factor of the closed-loop resonant poles of the inverter with the *HO*-filter also occurs at critical inductance L_{tcri}. A higher damping factor makes the satisfaction of the gain margin requirements become much easier. Therefore, it is only necessary to check the gain margins of the system under the critical grid condition. If the requirements (3dB or $-$ 3dB) of the gain margins are not satisfied, then the designer should go back to step 2 to reduce K_p until the gain margins are met.

Fig. 11 shows the step-by-step procedure for the hybrid damping design of the *HO*-filter-based inverter.

E. Effect of ESRs on System

The ESRs of the filter are neglected in the aforementioned analysis to emulate the worst operating conditions. But it has a great effect on the stability of the system in reality. For a better analysis on the efficiency of the proposed design method in the following experiments, a brief analysis on the effect of ESRs on system is necessary. Fig. 12 shows the Bode plots of open-loop transfer function of the undamped system with different ESRs values. $R_1 = 0.011\ \Omega$ and $R_2 = 0.015\ \Omega$ are considered here. As shown in Fig. 12, there are three characteristic resonant frequencies for the *HO*-filter-based inverter, and the minimal ESRs damp the resonances well and system becomes barely stable without additional damping method.

IV. Design Example

Design examples are presented in this section to make an intuitive understanding of the proposed method. Table I gives the parameters of a 65-kW three-phase *HO*-filter-based grid-connected inverter. The parameters are regularly designed with the method proposed in [30]. To generalize guidelines for

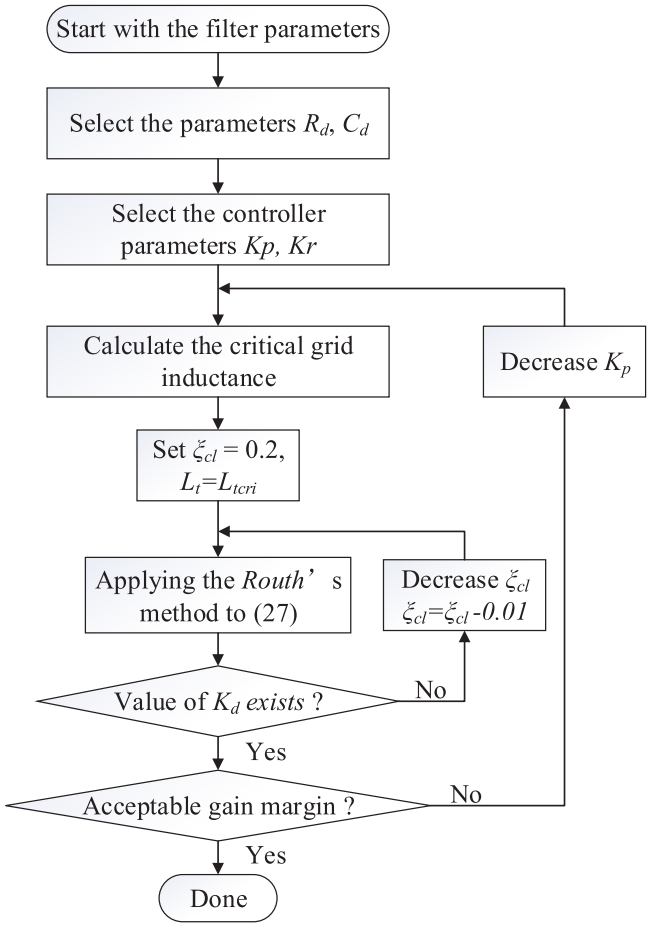

Fig. 11. Design flow for the hybrid damping design of the *HO*-filter-based inverter.

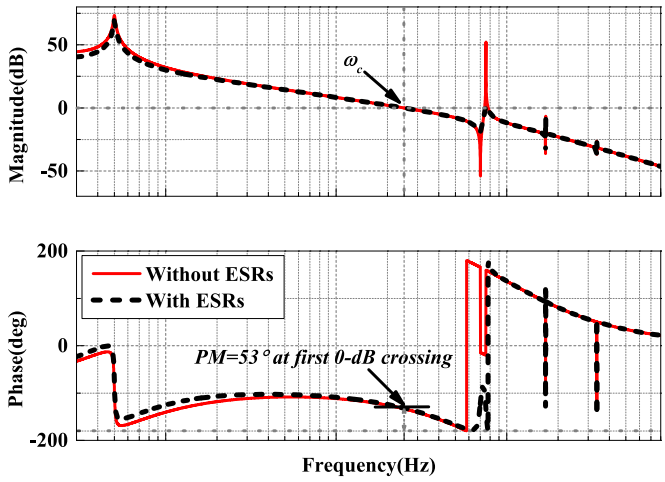

Fig. 12. Bode plots of open-loop transfer function of the *HO*-filter-based inverter without damping under the stiffest grid condition.

selecting optimum damping parameters, per unit approach is adopted, which could be extended to any power rating/voltage rating.

1) As shown in the Table I, there are two trap filter branches, whose *LC* resonant frequencies are 16 and 32 kHz, respectively. Based on the equivalent circuit analysis method, C_{eq1} can be derived as 0.00227 p.u., and C_{eq2} is derived as 0.0018 p.u. Using (8), the equivalent capacitance C' can be obtained as 0.01757 p.u. With the equivalent *LCL*-filter parameters and different values of R_d, multiple diagrams that reflect the variation of *Q-factor* and power loss, w.r.t., a_C can be plotted according to (11) and (15). There is no improvement in the *Q-factor* if a_C is increased beyond 0.5 in this case. Here, we set $a_C = 0.5$ as the best choice ($C_d = 0.0067$ p.u.). The resistor of the passive damper is chosen as 2.5 p.u. according to (22) ($R_d \geq 2.25$ p.u.) under the weakest grid condition. The maximum value of 0.5 p.u. (4 mH) is selected considering the line impedance in a weak grid and the presence of many parallel inverters.
2) To yield satisfactory transient performance, a phase margin of $PM = 45^\circ$ at $\omega_c \approx 0.3\omega_r^{LCL}$ is desired. With the selected passive damping parameters, the ω_r^{LCL} can be calculated as 4 8444 rad/s according to (17) when $L_g = 0$. Applying (23) and (24) to the system gives controller gains of $K_p = 2.2$ and $K_r = 500$.
3) The critical grid inductance is calculated from (27), $L_{\mathrm{tcri}} = 0.018$ p.u. (140 μH). This is consistent with the outcome from [31] that if $L_t > L_1$ or $L_t \approx L_1$, high-frequency current oscillations increase through the internal loop, raising the ratings of the switches. Therefore, the conclusion can be used as a constraint when designing the filter.
4) The pole localization algorithm stops at $\xi_{cl} = 0.15$. The satisfactory range of K_d can be calculated as $(-0.76, -0.33)$. In order to obtain the best damping performance, it is better to choose the intermediate value of this range. Here, $K_d = -0.5$ is chosen.
5) As shown in Fig. 13, the minimal damping factor of the closed-loop resonant poles of the *HO*-filter-based inverter also occurs at $L_t = 0.018$ p.u.. This is consistent with the previous analysis, and it proves the effectiveness of the proposed equivalent circuit analysis method. The gain margin around the resonance is 5.5 dB as shown in Fig. 14 (no open-loop unstable poles), which can meet the requirement of the design specification.

TABLE I
PARAMETERS OF THE PROTOTYPE IN ABSOLUTE AND P.U. VALUES

System Parameters			
Parameter	Value	Parameter	Value
Grid voltage V_g (RMS)	230 V	Fundamental frequency f_0	50 Hz
Rated power P_{rated}	65 kW	Switching frequency f_{sw}	16 kHz
Dc-link voltage V_{dc}	800 V	Sampling frequency f_s	32 kHz
HO-filter Parameters			
Inverter-side inductor L_1	120 μH 0.0154	Grid-side inductor L_2	20 μH 0.0026
Trap inductor 1 L_{f1}	45 μH 0.0058	Trap inductor 2 L_{f2}	11.3 μH 0.0015
Trap capacitor 1 C_1	2.2 μF 0.0017	Trap capacitor 2 C_2	2.2 μF 0.0017
Filter capacitor C_f	17.6 μF 0.0135		

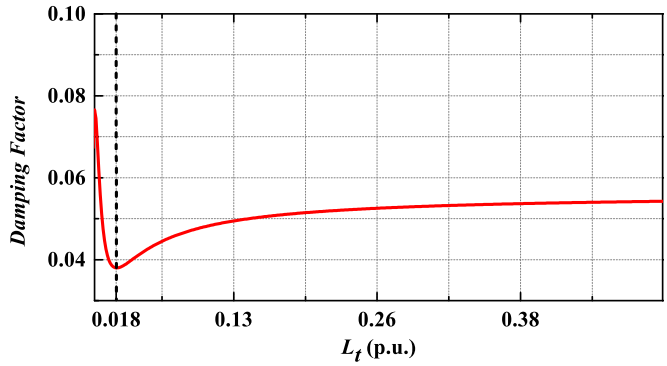

Fig. 13. Curves of the damping factor of the closed-loop poles with increase in L_t.

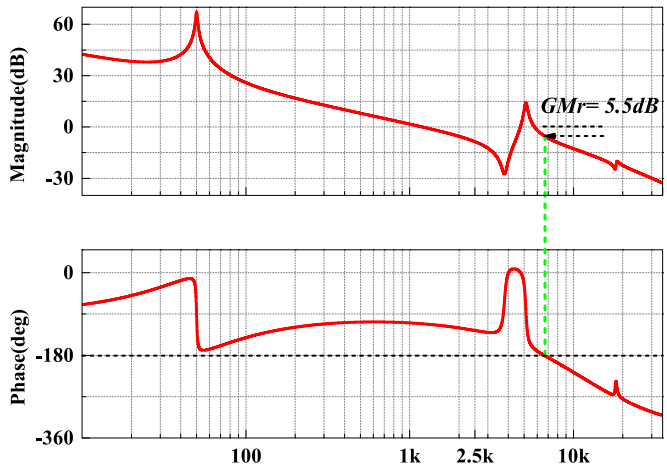

Fig. 14. Bode plot of the open-loop transfer function when $L_t = 0.018$ p.u..

V. Experimental Verification

The experimental system consists of a 65-kW three-phase prototype inverter based on FPGA (EP4CE115F780), which is connected to the grid through an *HO*-filter, and the configuration is shown in Fig. 3. Fig. 15 shows the prototype construction. The system operates as a reactive current generator with dc bus voltage regulation. Note that the *HO*-filter-based inverter is connected to the real grid through a locally isolated transformer, whose leakage inductor of the transformer (0.0013 p.u.) works as a part of L_g, and another part of the grid impedance is emulated by an external inductor. All the parameters are the same as those of the theoretical analysis in Section IV.

Fig. 16 shows the experimental results under a full-load condition without damping when $L_g = 0.0013$ p.u. As shown in Fig. 16, the system is barely stable and the output oscillates around 6 kHz. It is possible to run the system without damping under the stiffest grid condition due to the ESRs and natural passive resonance damping of the filter itself. This is consistent with the previous analysis.

Fig. 17 shows the experimental results under a full-load condition with hybrid damping. For $L_g = 0.0013$ p.u. and $L_g = 0.5$ p.u., the satisfactory stable operations are maintained

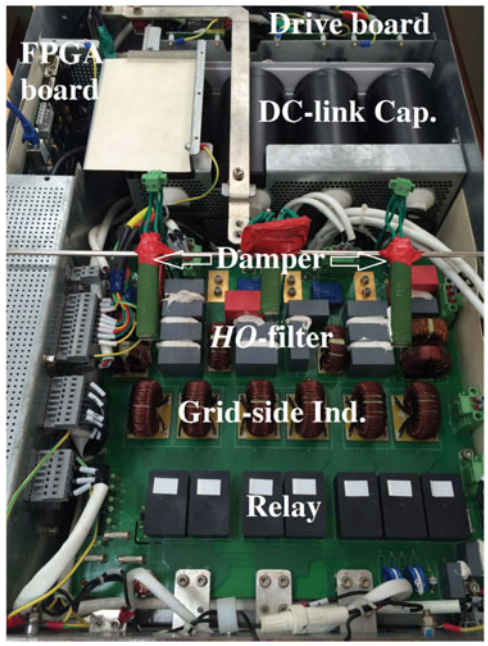

Fig. 15. Photograph of the three-phase grid-connected inverter prototype.

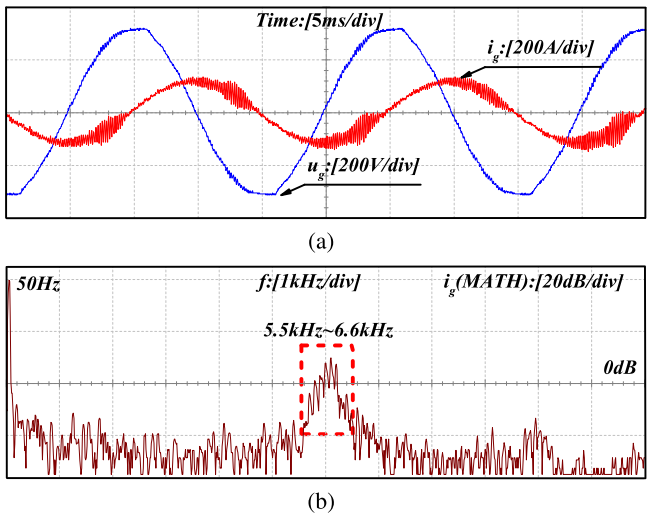

Fig. 16. Experimental results under a full-load condition without damping in the stiffest grid ($L_g = 0.0013$ p.u.). (a) Grid voltage and grid-side current. (b) Fast Fourier transform (FFT) of the grid-side current.

for both passive damping and hybrid damping as shown in Fig. 17(a) and (c). For $L_g = 0.0143$ p.u. ($L_t = 0.018$ p.u.), as shown in Fig. 17(b), when active damping is disabled, disastrous oscillation is triggered. This demonstrates that the designed parameters perform with high robustness against the grid impedance variation. Fig. 17(a) and (c) also show the measured rms value of the current of $R_d - C_d$ branch. It can be calculated that the power loss at the *RC*-parallel damper is limited to $1.61^2 \cdot R_d/P_{\text{rated}} = 0.00024$ p.u., where P_{rated} is the power rating of the prototype system. This result is consistent with the theoretical analysis, as shown in Fig. 6 (about 0.0005 p.u.).

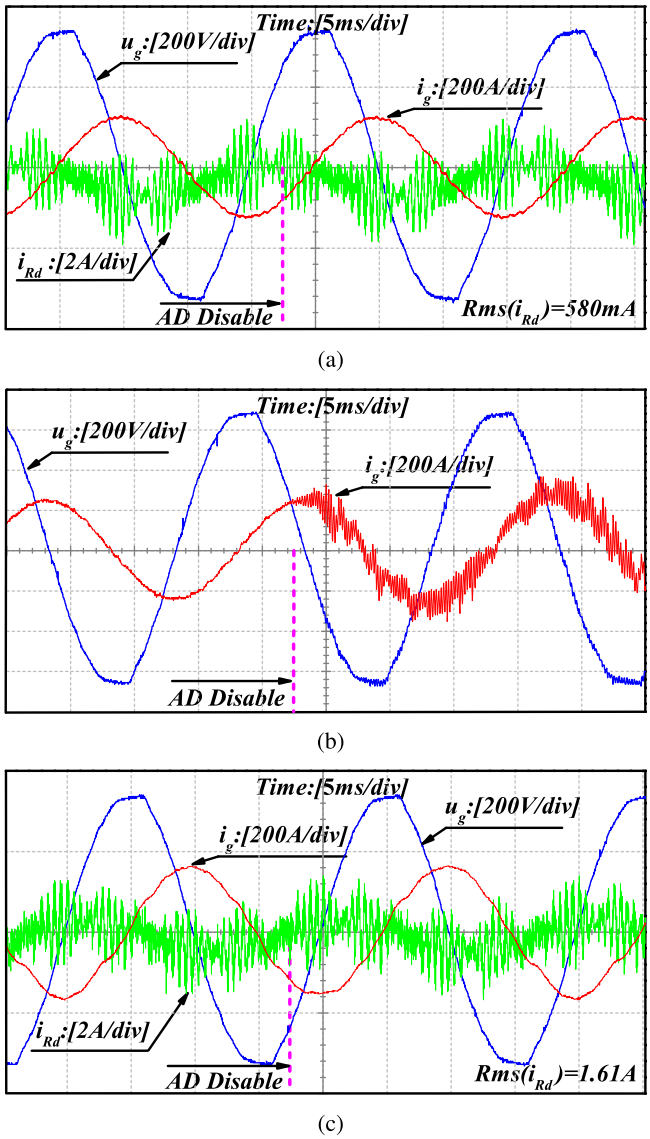

Fig. 17. Measured grid voltage and grid-side current under a full-load condition with hybrid damping and the active damping is disabled at a certain moment. (a) Under the stiffest grid condition ($L_g = 0.0013$ p.u.). (b) Under the critical grid condition ($L_g = 0.0143$ p.u.). (c) Under the weakest grid condition ($L_g = 0.5$ p.u.).

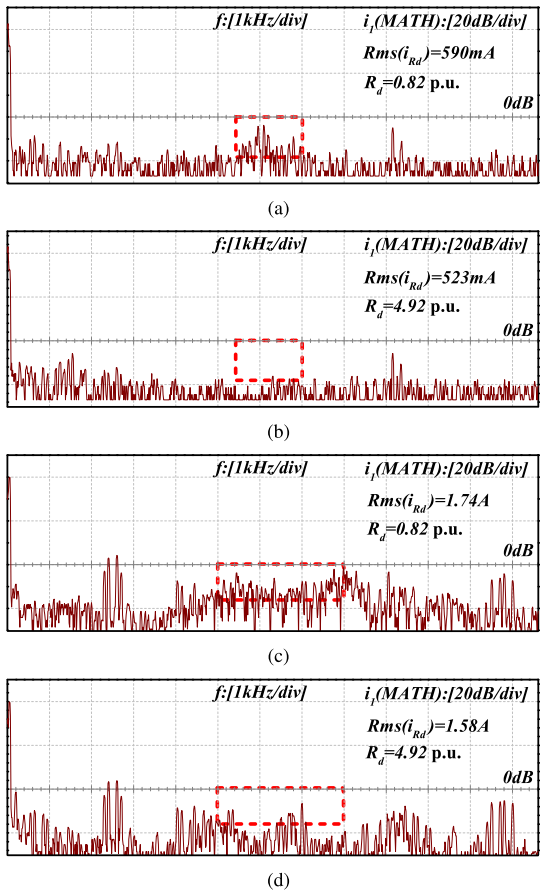

Fig. 18. Measured FFT of the inverter-side current under a full-load condition with hybrid damping. (a) Under the stiffest grid condition ($L_g = 0.0013$ p.u.) when $R_d = 0.82$ p.u. (b) Under the stiffest grid condition ($L_g = 0.0013$ p.u.) when $R_d = 4.92$ p.u. (c) Under the weakest grid condition ($L_g = 0.5$ p.u.) when $R_d = 0.82$ p.u. (d) Under the weakest grid condition ($L_g = 0.5$ p.u.) when $R_d = 4.92$ p.u.

Fig. 18 shows the experimental results when varying the value of the damping resistor. If the damping resistor is set to $R_d = 0.82$ p.u., the resonant current is increased and the power loss is limited to $1.74^2 \cdot R_d/P_{\text{rated}} = 0.000093$ p.u. However, a larger damping resistor R_d of 4.92 p.u. results in larger power loss ($1.58^2 \cdot R_d/P_{\text{rated}} = 0.00046$ p.u.). Hence, a damping resistor R_d of 2.5 p.u. achieves a good balance between the damping effect and damping losses.

Fig. 19 shows the measured waveforms of inverter-side current and its corresponding FFT analysis. The results demonstrates that, compared with other alternative interfacing filters, the *HO*-filter described in this paper can better attenuate the harmonics around the multiples of switching frequencies and guarantee -60 dB/decade attenuation in the high-frequency band with lower inductance.

Fig. 20 shows the transient experimental results when the current reference steps from half- to full-load. It is seen that the process is smooth with little overshoot.

In the experiments, when only active damping is adopted under the critical grid, significant oscillation also arises in the grid current. When K_p is reduced in the critical grid condition with only passive damping or active damping, the output current of inverter contains no oscillations as shown in Fig. 21 [see also Fig. 17(b)]. However, the transient responses become slower, and the rejection of low-order harmonics is weakened compared with Fig. 20(b). Therefore, in order to improve the speed of the transient response, the damping factor of the closed-loop resonant poles has to be selected as large as possible. The sufficiently damped resonant poles assume a larger K_p. Experimental testing has proven the effectiveness of the design method in ensuring smooth and fast transient response.

To enhance the disturbance rejection performance, proportional harmonic resonant controllers are applied, to provide internal model dynamics at selected harmonic frequencies. When the grid voltage is distorted by the 3rd (3.4% w.r.t. the grid fundamental voltage), 5th, 7th, 9th, and 11th harmonics, grid voltage u_g and grid-side current i_g in the weakest grid are shown in

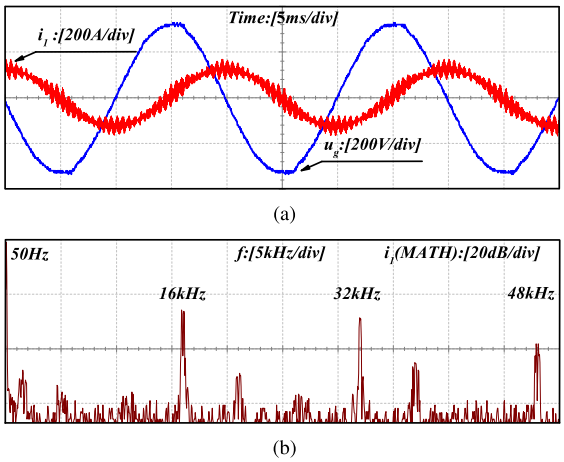

Fig. 19. Experimental results under a full-load condition with hybrid damping in the stiffest grid ($L_g = 0.0013$ p.u.). (a) Grid voltage and inverter-side current. (b) FFT of the inverter-side current.

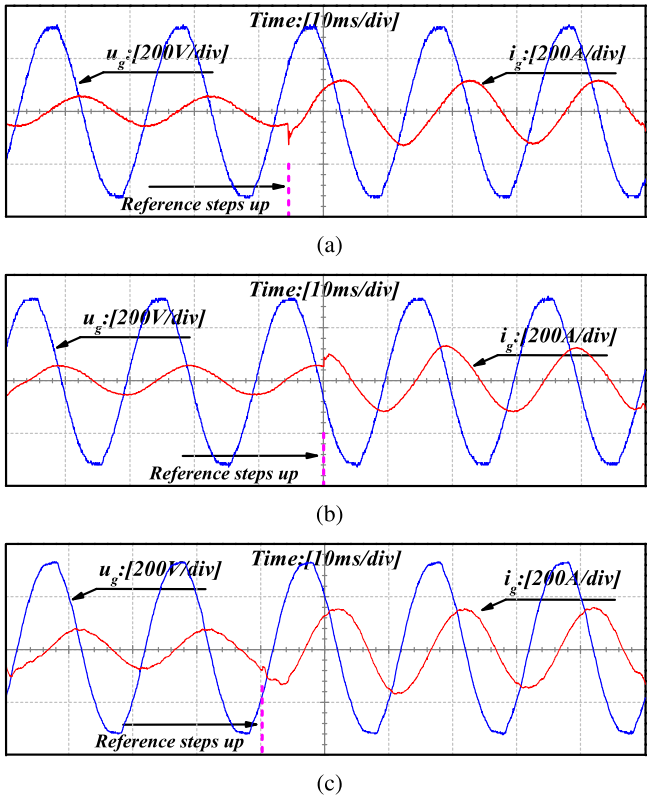

Fig. 20. Measured grid voltage and grid-side current when the current reference steps from half- to full-load with hybrid damping. (a) Under the stiffest grid condition ($L_g = 0.0013$ p.u.). (b) Under the critical grid condition ($L_g = 0.0143$ p.u.). (c) Under the weakest grid condition ($L_g = 0.5$ p.u.).

Fig. 22(a). Fig. 22(b) shows the FFTs of u_g and i_g. It can be found that the system can be kept stable and can suppress up to the 11th harmonic well. In the low frequency range, the most challenging issue is to have enough bandwidth to plug in the harmonic resonant controllers. Therefore, the experimental results confirm the effectiveness of the proposed design method in achieving a desired control bandwidth.

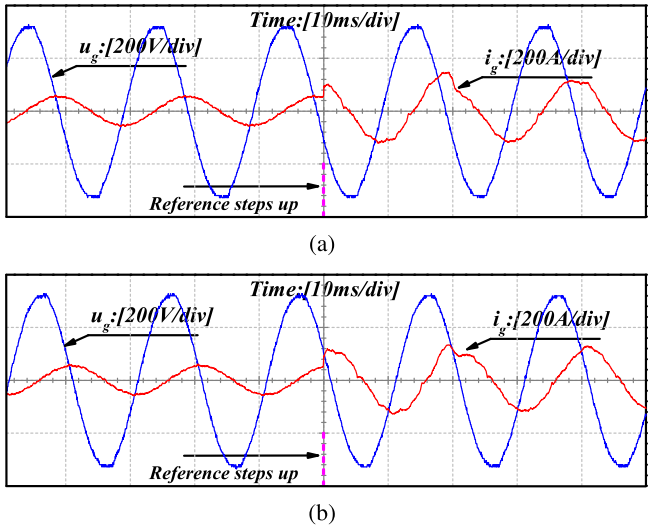

Fig. 21. Measured grid voltage and grid-side current under the critical grid ($L_g = 0.0143$ p.u.) with reduced K_p when the current reference steps from half- to full load. (a) With only passive damping ($K_p = 0.6$). (b) With only active damping ($K_p = 0.8$).

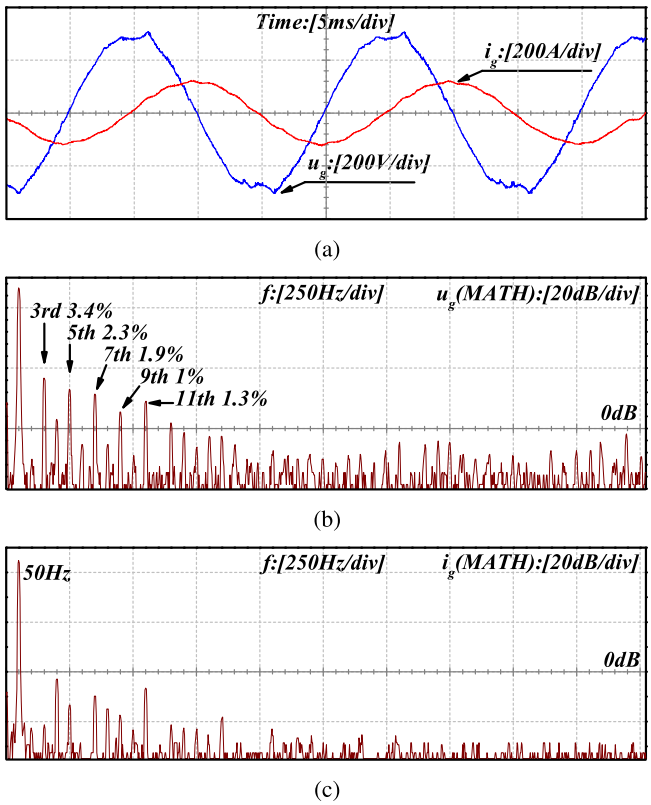

Fig. 22. Experimental results under a full-load condition with hybrid damping when the harmonics are injected into the grid voltage in the weakest grid ($L_g = 0.5$ p.u.). (a) Grid voltage and grid-side current waveforms. (b) FFT of the grid voltage. (c) FFT of the grid-side current.

We also have studied the prototype in stand-alone mode ($L_g = 0$). For $L_g = 0$, as shown in Fig. 23, the grid voltage does not contain harmonics, and satisfactory stable operations are maintained.

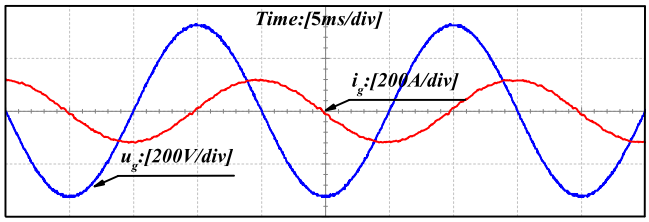

Fig. 23. Measured grid voltage and grid-side current in the stand-alone mode ($L_g = 0$) with hybrid damping.

With the weakest grid or stiffest grid, the system operates with good stability margin by only using active damping or passive damping. The experimental waveforms of active damping and passive damping under the weakest grid or stiffest grid are highly similar to those of hybrid damping and not repeated in this paper.

VI. Conclusion

This paper presented a systematic design method for hybrid damping in *HO*-filter based inverters. The design method has been generalized and can be applied for any ratings of the *HO*-filter and can stabilize the system with a wide variation range of grid impedance values without sacrificing efficiency of the system. A simple equivalent circuit analysis method is proposed to simplify the model of the *HO*-filter. With this method, the resonant frequency and the *Q-factor* of the *RC*-damped *HO*-filter can be easily calculated. A practical method is proposed to calculate the critical grid inductance of the *RC*-damped system with inverter-current feedback. A simple iterative algorithm has been proposed based on damping factor. This method can maximize the performance of the hybrid damping due to that it can accurately locate the position of the resonant poles. Experimental results of a 65-kW prototype verify the effectiveness of the proposed design method and validity of the analysis.

References

[1] F. Blaabjerg, R. Teodorescu, M. Liserre, and A. Timbus, "Overview of control and grid synchronization for distributed power generation systems," *IEEE Trans. Ind. Electron.*, vol. 53, no. 5, pp. 1398–1409, Oct. 2006.

[2] M. Liserre, F. Blaabjerg, and S. Hansen, "Design and control of an *LCL*-filter-based three-phase active rectifier," *IEEE Trans. Ind. Appl.*, vol. 41, no. 5, pp. 1281–1291, Sep. 2005.

[3] J. Xu, J. Yang, J. Ye, Z. Zhang, and A. Shen, "An *LTCL* filter for three-phase grid-connected converters," *IEEE Trans. Power Electron.*, vol. 29, no. 8, pp. 4322–4338, Aug. 2014.

[4] F. Li, X. Zhang, H. Zhu, H. Li, and C. Yu, "An *LCL-LC* filter for grid-connected converter: Topology, parameter, and analysis," *IEEE Trans. Power Electron.*, vol. 30, no. 9, pp. 5067–5077, Sep. 2015.

[5] W. Wu, Y. He, T. Tang, and F. Blaabjerg, "A new design method for the passive damped *LCL* and *LLCL* filter-based single-phase grid-tied inverter," *IEEE Trans. Ind. Electron.*, vol. 60, no. 10, pp. 4339–4350, Oct. 2013.

[6] P. Channegowda and V. John, "Filter optimization for grid interactive voltage source inverters," *IEEE Trans. Ind. Electron.*, vol. 57, no. 12, pp. 4106–4114, Dec. 2010.

[7] R. N. Beres, X. Wang, F. Blaabjerg, M. Liserre, and C. L. Bak, "Optimal design of high-order passive-damped filters for grid-connected applications," *IEEE Trans. Power Electron.*, vol. 31, no. 3, pp. 2083–2098, Mar. 2016.

[8] Y. Liu, W. Wu, Y. He, Z. Lin, F. Blaabjerg, and H. S.-H. Chung, "An efficient and robust hybrid damper for *LCL*- or *LLCL*-based grid-tied inverter with strong grid-side harmonic voltage effect rejection," *IEEE Trans. Ind. Electron.*, vol. 63, no. 2, pp. 926–936, Feb. 2016.

[9] X. Wang, F. Blaabjerg, and P. C. Loh, "Virtual *RC* damping of *LCL*-filtered voltage source converters with extended selective harmonic compensation," *IEEE Trans. Power Electron.*, vol. 30, no. 9, pp. 4726–4737, Sep. 2015.

[10] R. Pena-Alzola, M. Liserre, F. Blaabjerg, R. Sebastián, J. Dannehl, and F. W. Fuchs, "Systematic design of the lead-lag network method for active damping in *LCL*-filter based three phase converters," *IEEE Trans. Ind. Informat.*, vol. 10, no. 1, pp. 43–52, Feb. 2014.

[11] M. Malinowski and S. Bernet, "A simple voltage sensorless active damping scheme for three-phase PWM converters with an filter," *IEEE Trans. Ind. Electron.*, vol. 55, no. 4, pp. 1876–1880, Apr. 2008.

[12] J. Dannehl, F. W. Fuchs, S. Hansen, and P. B. Thogersen, "Investigation of active damping approaches for PI-based current control of grid-connected pulse width modulation converters with LCL filters," *IEEE Trans. Ind. Appl.*, vol. 46, no. 4, pp. 1509–1517, Jul./Aug. 2010.

[13] D. Pan, X. Ruan, C. Bao, W. Li, and X. Wang, "Optimized controller design for-type grid-connected inverter to achieve high robustness against grid-impedance variation," *IEEE Trans. Ind. Electron.*, vol. 62, no. 3, pp. 1537–1547, Mar. 2015.

[14] F. Liu, Y. Zhou, S. Duan, J. Yin, B. Liu, and F. Liu, "Parameter design of a two-current-loop controller used in a grid-connected inverter system with LCL filter," *IEEE Trans. Ind. Electron.*, vol. 56, no. 11, pp. 4483–4491, Nov. 2009.

[15] Y. Tang, P. C. Loh, P. Wang, F. H. Choo, and F. Gao, "Exploring inherent damping characteristic of LCL-filters for three-phase grid-connected voltage source inverters," *IEEE Trans. Power Electron.*, vol. 27, no. 3, pp. 1433–1443, Mar. 2012.

[16] C. Bao, X. Ruan, X. Wang, W. Li, D. Pan, and K. Weng, "Step-by-step controller design for *LCL*-type grid-connected inverter with capacitor–current-feedback active-damping," *IEEE Trans. Power Electron.*, vol. 29, no. 3, pp. 1239–1253, Mar. 2014.

[17] D. Pan, X. Ruan, C. Bao, W. Li, and X. Wang, "Capacitor-current-feedback active damping with reduced computation delay for improving robustness of LCL-type grid-connected inverter," *IEEE Trans. Power Electron.*, vol. 29, no. 7, pp. 3414–3427, Jul. 2014.

[18] J. Dannehl, M. Liserre, and F. W. Fuchs, "Filter-based active damping of voltage source converters with *LCL* filter," *IEEE Trans. Ind. Electron.*, vol. 58, no. 8, pp. 3623–3633, Aug. 2011.

[19] R. Pena-Alzola, M. Liserre, F. Blaabjerg, M. Ordonez, and T. Kerekes, "A self-commissioning notch filter for active damping in a three-phase *LCL*-filter-based grid-tie converter," *IEEE Trans. Power Electron.*, vol. 29, no. 12, pp. 6754–6761, Dec. 2014.

[20] M. Liserre, A. Dell'Aquila, and F. Blaabjerg, "Genetic algorithm-based design of the active damping for an LCL-filter three-phase active rectifier," *IEEE Trans. Power Electron.*, vol. 19, no. 1, pp. 76–86, Jan. 2004.

[21] J. Dannehl, C. Wessels, and F. W. Fuchs, "Limitations of voltage-oriented PI current control of grid-connected PWM rectifiers with filters," *IEEE Trans. Ind. Electron.*, vol. 56, no. 2, pp. 380–388, Feb. 2009.

[22] N. Mukherjee and D. De, "Analysis and improvement of performance in *LCL* filter-based PWM rectifier/inverter application using hybrid damping approach," *IET Trans. Power Electron.*, vol. 6, no. 2, pp. 309–325, Feb. 2013.

[23] M. Liserre, R. Teodorescu, and F. Blaabjerg, "Stability of photovoltaic and wind turbine grid-connected inverters for a large set of grid impedance values," *IEEE Trans. Power Electron.*, vol. 21, no. 1, pp. 263–272, Jan. 2006.

[24] J. J. D'Azzo, S. N. Sheldon, and C. H. Houpis, *Linear Control System Analysis and Design With MATLAB*, 5th ed. New York, NY, USA: Marcel Dekker, 2003.

[25] Y. Tang, P. C. Loh, P. Wang, F. H. Choo, F. Gao, and F. Blaabjerg, "Generalized design of high performance shunt active power filter with output *LCL* filter," *IEEE Trans. Ind. Electron.*, vol. 59, no. 3, pp. 1443–1452, Mar. 2012.

[26] D. G. Holmes and T. A. Lipo, *Pulse Width Modulation for Power Converters: Principles and Practice*. New York, NY, USA: Wiley, 2003, vol. 18.

[27] R. Pena-Alzola, M. Liserre, F. Blaabjerg, M. Ordonez, and Y. Yang, "*LCL*-filter design for robust active damping in grid-connected converters," *IEEE Trans. Ind. Informat.*, vol. 10, no. 4, pp. 2192–2203, Nov. 2014.

[28] D. Holmes, T. Lipo, B. McGrath, and W. Kong, "Optimized design of stationary frame three phase AC current regulators," *IEEE Trans. Power Electron.*, vol. 24, no. 11, pp. 2417–2426, Nov. 2009.

[29] W. Wu *et al.*, "A robust passive damping method for *LLCL*-filter-based grid-tied inverters to minimize the effect of grid harmonic voltages," *IEEE Trans. Power Electron.*, vol. 29, no. 7, pp. 3279–3289, Jul. 2014.
[30] W. Wu, Y. He, and F. Blaabjerg, "An LLCL power filter for single-phase grid-tied inverter," *IEEE Trans. Power Electron.*, vol. 27, no. 2, pp. 782–789, Feb. 2012.
[31] M. T. Bina and E. Pashajavid, "An efficient procedure to design passive LCL-Filters for active power filters," *Elect. Power Syst. Res.*, vol. 79, no. 4, pp. 606–614, 2009.

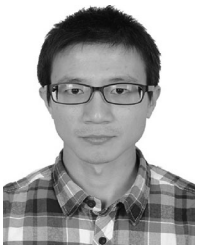

Jie Ye was born in Hubei, China, in 1989. He received the B.S. degree from the Department of Software Engineering, Xidian University, Xian, China, in 2011. He is currently working toward the Ph.D. degree with the School of Automation, Huazhong University of Science and Technology, Wuhan, China.

He is involved in research on the signal process and circuit theory, as well as harmonics suppression and reactive power compensation.

Anwen Shen received the B.S. and M.S. degree from Zhejiang University, Zhejiang, China, in 1991 and 1994, respectively, and the Ph.D. degree from the Huazhong University of Science and Technology (HUST), Wuhan, China, in 1997, all in automation.

In 1997, he joined the Department of Control Science and Engineering, HUST, where he is currently a Professor in the School of Automation. He is a holder of more than ten patents, and several of them have been commercialized. His research interests include advanced motion control, power electronic application, motor drives, electrical vehicles, and intelligent control.

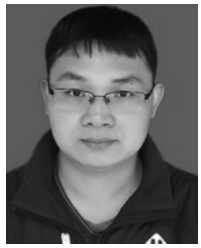

Zhixiong Zhang was born in Hubei, China, in 1983. He received the B.S. degree from the Department of Electronics and Information Engineering, Huazhong University of Science and Technology, wuhan, China, in 2006, where he is currently working toward the Ph.D. degree with the School of Automation.

His research interests include power electronics, signal process, and circuit theory.

Jinbang Xu was born in Hubei, China, in 1973. He received the Ph.D. degree in control science and engineering from the Department of Control Science and Engineering, Huazhong University of Science and Technology (HUST), Wuhan, China, in 2004.

He is currently a professional with the School of Automation, HUST. His research interests include power electronics, intelligent control, and bioinformatics processing.

Fang Wu was born in Hunan, China, in 1988. He received the B.S. degree from the School of Electrical and Information Engineering, Hunan University, Changsha, China, in 2011. He is currently working toward the Ph.D. degree in the Department of Control Science and Engineering, School of Automation, Huazhong University of Science and Technology, Wuhan, China.

His research interests include power electronics, active power filter, intelligent control, and power conversion.